Isotropic, nematic, and lamellar phases in colloidal suspensions of nanosheets

Patrick Davidson[a,1], Christophe Penisson[b,c], Doru Constantin[a], and Jean-Christophe P. Gabriel[c,1]

[a]Laboratoire de Physique des Solides, CNRS, Université Paris-Sud, Université Paris-Saclay, 91405 Orsay Cedex, France; [b]ICSM (Institut de Chimie Séparative de Marcoule), UMR 5257 Commissariat à l'énergie atomique et aux énergies alternatives (CEA)/CNRS/École Nationale Supérieure de Chimie de Montpellier, Université de Montpellier, 30207 Bagnols sur Cèze, France; and [c]University Grenoble Alpes, CEA, Institut Nanosciences et Cryogénie, Modélisation et Exploration des Matériaux, 38000 Grenoble, France

Edited by Thomas E. Mallouk, The Pennsylvania State University, University Park, PA, and approved May 15, 2018 (received for review February 13, 2018)

The phase diagram of colloidal suspensions of electrically charged nanosheets, such as clays, despite their many industrial uses, is not yet understood either experimentally or theoretically. When the nanosheet diameter is very large (∼100 nm to 1 μm), it is quite challenging to distinguish the lamellar liquid-crystalline phase from a nematic phase with strong stacking local order, often called "columnar" nematic. We show here that newly upgraded small-angle X-ray scattering beamlines at synchrotron radiation facilities provide high-resolution measurements which allow us to identify both phases unambiguously, provided that single domains can be obtained. We investigated dilute aqueous suspensions of synthetic $Sb_3P_2O_{14}^{3-}$ nanosheets that self-organize into two distinct liquid-crystalline phases, sometimes coexisting in the same sample. Close examination of their X-ray reflection profiles in the directions perpendicular to the director demonstrates that these two mesophases are a columnar nematic and a lamellar phase. In the latter, the domain size reaches up to ∼20 μm, which means that each layer is made of >600 nanosheets. Because the lamellar phase was only rarely predicted in suspensions of charged disks, our results show that these systems should be revisited by theory or simulations. The unexpected stability of the lamellar phase also suggests that the rims and faces of $Sb_3P_2O_{14}^{3-}$ nanosheets may have different properties, giving them a patchy particle character.

liquid crystals | nanosheets | X-ray scattering | colloids | lamellar

Colloidal suspensions of anisotropic nanoparticles are presently raising renewed interest because they are good model systems for studying the appearance of liquid-crystalline phases (1). Although the behavior of rod-like nanoparticles undergoing either hard-core or electrostatic interactions has been largely explored (2–9), the case of disk-like nanoparticles stabilized through electrostatic repulsions, in polar solvents like water, still remains unclear, even from a theoretical point of view (10, 11). This could hinder the wide industrial application of these colloidal suspensions which are used in domains ranging from oil recovery to cosmetics. In principle, in addition to the usual isotropic liquid phase and the liquid-crystalline nematic phase, which has long-range orientational order, suspensions of disk-like particles can self-organize in lamellar and columnar phases which have long-range positional order in one and two dimensions, respectively (1). The free energies of these latter two mesophases are often predicted to be so close that the occurrence of one or other phase may depend on subtle specific microscopic parameters and interactions. Moreover, nanoparticles with a very large aspect ratio (>100), called nanosheets hereafter, such as clay, dichalcogenide, graphene, or other inorganic systems (12–19), raise questions that are difficult to tackle experimentally. For example, each layer of the lamellar phase must be made of more or less parallel nanosheets located in the same layer plane, which is difficult to demonstrate. In the more classical cases of the SmA phase of molecular thermotropic liquid crystals and the L_α phase of surfactant molecules (without which life, as we know it, would not exist, because they are the prime constituent of all cell membranes), such lamellar self-assembly spontaneously proceeds from the segregation of amphipathic parts of the molecules (1). Once the segregation sets in, layers form and grow until they reach the sample boundaries or are limited by topological defects. This self-assembly mechanism driven by molecular segregation cannot be invoked for these mineral liquid crystals based on colloidal suspensions of nanosheets (20). The stability of the lamellar phase must then proceed either from purely entropic interactions, such as excluded-volume interactions, or from electrostatic repulsions, or even from more specific effects such as differences, at the microscopic scale, between the faces and the rims of the nanosheets.

Investigating the microscopic structure of colloidal suspensions of nanosheets, in situ, by optical microscopy is actually quite challenging because the particles have very little optical contrast because they are small and thin (∼500-nm diameter and ∼1 nm thick), and they are not fluorescent. Moreover, the usual electron microscopy and atomic force microscopy techniques require sample preparation that may affect the structure. The most common and arguably best suited technique for this purpose is X-ray scattering, but probing in detail the relative positions of nanosheets within layers requires the production of an aligned sample of lamellar phase. Moreover, investigating its structure over length scales of typically 10 μm requires excellent instrumental resolution while maintaining large enough beam intensity. The recent upgrade of

Significance

Colloidal suspensions of electrically charged nanometric sheets (nanosheets), like graphene oxide or clays, which are widely used in industry, form liquid-crystalline phases. These include the nematic phase, where all nanosheets are approximately parallel, and the lamellar phase, where they also form equidistant layers. When the particle diameter is large (100 nm to 1 μm), distinguishing these phases is quite challenging. Using newly available synchrotron small-angle X-ray scattering setups, we unambiguously identified both phases, in $H_3Sb_3P_2O_{14}$ nanosheet suspensions, by analyzing their X-ray scattering patterns. The lamellar domain size reaches 20 μm, which means each layer is made of ∼1,000 nanosheets. Because the lamellar phase was rarely predicted in suspensions of charged disks, these systems should be revisited by theory or simulations.

Author contributions: P.D. and J.-C.P.G. designed research; P.D., C.P., D.C., and J.-C.P.G. performed research; P.D., C.P., D.C., and J.-C.P.G. analyzed data; and P.D. and J.-C.P.G. wrote the paper.

The authors declare no conflict of interest.

This article is a PNAS Direct Submission.

[1]To whom correspondence may be addressed. Email: patrick.davidson@u-psud.fr or jean-christophe.gabriel@cea.fr.

This article contains supporting information online at www.pnas.org/lookup/suppl/doi:10.1073/pnas.1802692115/-/DCSupplemental.

Published online June 11, 2018.

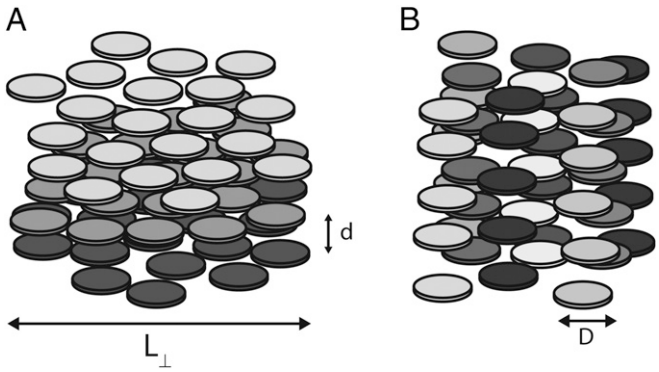

Fig. 1. Two possible types of organization of suspensions of nanosheets (depicted as small disks). (*A*) Lamellar phase: the nanosheets gather in equidistant layers. Nanosheets of the same gray shade belong to the same layer. d is the lamellar period, and $L_\perp$ is the size of the lamellar domain in the plane perpendicular to the director. (*B*) Columnar nematic phase: the nanosheets stack locally in columns. Nanosheets of the same gray shade show short-range stacking positional order and belong to the same column. D is the nanosheet diameter.

third-generation synchrotron radiation facilities allowed us to perform such a study. We used an upgraded small-angle X-ray scattering (SAXS) beamline to distinguish a lamellar phase (Fig. 1*A*) from a so-called "columnar" nematic phase (Fig. 1*B*). This latter phase, of nematic symmetry, is made of disks which tend to stack over short distances and form short columns that align parallel to each other. We revisited the phase diagram of colloidal suspensions of synthetic $H_3Sb_3P_2O_{14}$ nanosheets (13), a material of interest for solid–liquid extraction of rare earth elements (21), and discovered that in addition to the isotropic liquid phase, many samples display two different coexisting mesophases that we identified as nematic and lamellar by high-resolution X-ray scattering. Our study also demonstrates that in the lamellar phase, the positional order of the nanosheets extends over a length scale of at least ∼20 μm and involves at least 600 nanosheets per layer.

Materials and Methods

Synthesis and Characterization (XRD). $H_3Sb_3P_2O_{14}$ was synthesized according to a previously published method (13). The synthesis was performed in two consecutive steps: the first high-temperature reaction led to the synthesis of $K_3Sb_3P_2O_{14}$, and the second led to the title compound by cation exchange in aqueous solution. For the synthesis of $K_3Sb_3P_2O_{14}$, a stoichiometric mixture of $NH_4H_2PO_4$ (23 mmol, 2.65 g, synthesized from mixing stoichiometric amounts of H_3PO_4 85 wt % in water with NH_3 30 wt % in water), Sb_2O_3 (17 mmol, 5.06 g; Merck), and KNO_3 (34 mmol, 3.51 g; Prolabo) was placed in a platinum crucible and heated in air, first at 300 °C (ramp of 50 °C/h) for 10 h to decompose $NH_4H_2PO_4$, then at 1,000 °C (ramp of 50 °C/h) for 100 h, yielding 8.78 g (12 mmol; yield = 100%) of $K_3Sb_3P_2O_{14}$ (X-ray powder diffraction showed impurities level <1%).

For the second synthesis step, 3.4 g of $K_3Sb_3P_2O_{14}$ powder was thoroughly ground and stirred in a 0.33-L solution of 7.5 M nitric acid at 50 °C for 22 h. During this process, the solid was centrifuged (3,000 × *g*) and rinsed with 18 MΩ water a few times until a swelling of the solid was noticed. This procedure was repeated three times to ensure a complete exchange of the alkali metal cations for protons to yield $H_3Sb_3P_2O_{14}$ (over 98% potassium to proton exchange). It should be noted that after the last cation exchange and centrifugation, the solid was only rinsed once to avoid too much swelling.

Further purification of $H_3Sb_3P_2O_{14}$ was achieved according to the following procedure: the gel collected after cation exchange was placed in a regenerated cellulose tubular membrane (Cellu Sep, width 46 mm, thickness 28 μm, pore size 1 nm) and was subjected to dialysis in 18 MΩ water, replacing the water regularly, until the nitrate ion concentration decreased to less than 1 ppm (JBL, nitrate test). During this dialysis, the lamellar, protonated phosphatoantimonic acid $H_3Sb_3P_2O_{14}$ kept on swelling.

Size fractionation procedures were then applied by centrifuging, on a Heraeus Biofuge Primo centrifuge (Thermo Fisher Scientific), the stock suspension at 8,000 g for 86 h, in 50 mL Falcon polypropylene conical tubes, leading to five different size fractions from top to bottom, named A to E. All fractions were carefully removed one by one, from top to bottom, using a pipette. The bottom fraction E was very small and consisted of white and insoluble solid impurities; it was discarded. The top two fractions were both transparent liquids and were separated by an interface. When observed between crossed polarizers, the top fraction showed some flow birefringence when agitated, whereas the one underneath was permanently birefringent. Both fractions were concentrated by rotoevaporation, yielding fractions A and B, for the very top and second ones, respectively. The third fraction from the top, labeled C, was made of a thixotropic white gel. It was separated by two interfaces from fraction B over it and fraction D below it, the latter being a dense white gel. After a preliminary fast exploration of the phase diagram of each fraction, samples were prepared in glass test tubes by diluting the fractions, up to a dilution factor of 100, so as to span the concentration range of interest.

Thermogravimetric Analysis. The weight fractions of the suspensions were determined by thermogravimetric analysis (TGA) under N_2 (model no. TGA92 from SETARAM Inc.) by heating to 250 °C. All calcined materials collected after TGA were white, indicating that no organic contamination arose from the cellulosic dialysis membranes. Weight fractions for A to D were measured to be 1.01 wt %, 1.77 wt %, 1.95 wt %, and 5.63 wt %, respectively.

Atomic Force Microscopy. Nanosheets were imaged by atomic force microscopy (AFM) to determine their size. They appeared as irregular flat objects of 1.1 ± 0.2 nm thick [in agreement with the crystallographic thickness of 1.10 nm of a single $Sb_3P_2O_{14}^{3-}$ layer (13, 22)]. Approximating these objects as regular disks, their average equivalent diameters (and SDs), for fractions A to D, are 44 (31) nm, 660 (615) nm, 790 (395) nm, and 960 (490) nm, respectively. A typical AFM image is given in *SI Appendix*, Fig. S1*A*, and the whole size distributions for A to D are shown in *SI Appendix*, Fig. S1 *B*–*E*.

Optical Studies. Test tubes were filled with samples of different concentrations and were first observed with the naked eye, either in the natural light of an LED hand lamp shone from below the tubes or between crossed polarizers in transmission. Reported observations were made 6 mo after the dilutions were performed, which gave time for the samples to reach equilibrium. No significant evolution has been observed since.

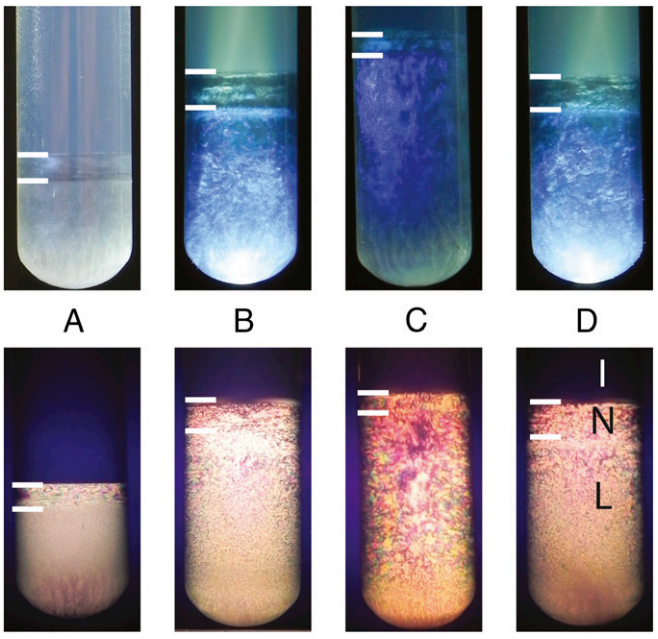

Fig. 2. Sample tubes photographed (*Top*) using LED light shone from below and (*Bottom*) directly viewed between crossed polarizers in transmission. All tubes were photographed 6 mo after initial dilution from the mother suspensions A, B, C, and D, with initial weight fractions (from left to right) of 1.01 wt %, 0.59 wt %, 0.79 wt %, and 0.57 wt %, respectively. White dashes have been superimposed on the tubes to indicate the location of visible interfaces (I, isotropic phase; L, lamellar phase; and N, nematic phase).

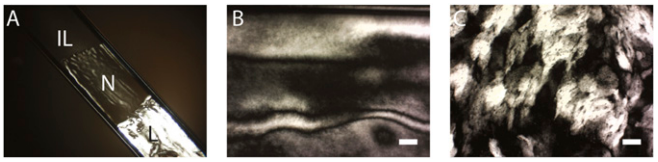

Fig. 3. Photographs of samples of $H_3Sb_3P_2O_{14}$ suspensions observed by polarized-light microscopy. (*A*) Suspension of nanosheets (size C, 0.35 wt %), showing three coexisting phases (IL, isotropic liquid; L, lamellar phase; and N, nematic phase) in a flat glass capillary. (The width of the capillary is 2 mm.) (*B*) Typical nematic texture of the intermediate phase (size A, the overall sample tube weight fraction is 0.51 wt %). (Scale bar, 100 μm.) (*C*) Texture of the bottom phase (size C, the overall sample tube weight fraction is 0.35 wt %). (Scale bar, 100 μm.) The polarizer and analyzer directions are parallel to the edges of the photographs.

Optical Microscopy. Polarized-light microscopy was performed with a BX51 microscope (Olympus) equipped with an Olympus digital camera. For texture observations, samples were filled in flat glass capillaries (Vitrocom) of 100- or 200-μm thickness, 2-mm width, and about 80-mm length. The capillaries were flame-sealed after filling and then stored vertically. Their evolution in time was monitored over several months, and they remained stable for more than a year.

SAXS Studies. Samples were inserted into cylindrical Lindemann glass capillaries of 1-mm diameter (Glas-Technik & Konstruktion) that were flame-sealed and left vertical in the field of gravity. Many of the X-ray capillaries were carefully scanned by X-ray scattering to characterize the different phases and to find areas where the X-ray beam impinged on only one (or a few) domain in reflection condition. One particular capillary was filled with a sample taken from a triphasic test tube (fraction C, 0.49 wt %) after remixing. Within 3 d, this sample appeared triphasic again and remained stable.

A first set of SAXS experiments were carried out at the SWING beamline of the SOLEIL synchrotron radiation facility. Measurements were made using a fixed energy of 12.0 keV and a sample-to-detector distance of 6.56 m. The typical accessible range of scattering vector modulus q was 10^{-2} to 1 nm^{-1} [$q = (4\pi/\lambda)\sin\theta$, where 2θ is the scattering angle and $\lambda = 0.1033$ nm is the wavelength]. Scattering patterns were recorded on an Aviex 170170 CCD camera formed with four detectors and placed in a vacuum detection tunnel. The pixel size was 41.7 μm, and the binning was either 2×2 or 4×4; the beam size at the detection level was about 50 μm. The scattering patterns were radially averaged to obtain the scattering curves I(q). The particular (fraction C, 0.49 wt %) capillary mentioned above was scanned by SAXS on SWING every 200 μm from its very bottom up to 28 mm above (well into the isotropic phase). The lamellar period, d, was obtained by using the relation $d = 2\pi/q_0$, where q_0 is the scattering vector modulus at the maximum of the reflection.

High-resolution SAXS experiments were also performed at the recently upgraded high-brilliance ID02 beamline of the European Synchrotron Radiation Facility in Grenoble, France (23). The X-ray energy was 12.48 keV ($\lambda = 0.0993$ nm), and the sample-to-detector distance was 20.007 m, which leads to an accessible q range of 0.005–0.15 nm^{-1}. The detector was a Frelon camera with pixel size of 24 μm. In high-resolution SAXS conditions, the instrumental resolution is mostly governed by the beam size at the detector level (120×120 μm^2). In reciprocal space, the resolution can be modeled as a Gaussian of full-width at half-maximum 2.7×10^{-4} nm^{-1}, which gave a coherence length of ~20 μm.

Results and Discussion

Observations of Samples with the Naked Eye. For all four size distributions A to D, some of the sample tubes clearly displayed two liquid–liquid interfaces that separated the liquid samples in three regions. [The A fraction already showed three phases at its initial synthesis (maximum) weight fraction of 1.01 wt %. B, C, and D remained monophasic down to 1.04, 0.84, and 0.81 wt %, respectively.] Typical triphasic sample tubes observed with the naked eye, either in natural light or between crossed polarizers, are shown in Fig. 2. The upper regions were clear and isotropic, but they always showed a strong flow birefringence at the slightest movement, especially near the top interface. Below this phase, a usually small birefringent region (5–15% of the overall height of the sample) was observed between two interfaces. The lowest phase was always birefringent and often displayed visible light diffraction, resulting in a blueish hue, as previously observed for the lamellar phase close to its maximum swelling periodicity (~ 200 nm) (13, 24). The appearance of three coexisting phases in samples of several centimeters height left under the influence of gravity is actually due to a vertical particle concentration gradient (evidence of this gradient was obtained by X-ray scattering; *SI Appendix*, Fig. S2). Such a phenomenon was already reported for colloidal suspensions of sterically stabilized gibbsite nanodisks in toluene (25). In this system of hard disks, the proportions of isotropic, nematic, and columnar phases were precisely modeled by balancing the effect of gravity with osmotic pressure. The gravitational length scale of $Sb_3P_2O_{14}^{3-}$ nanosheets, $l_g = k_BT/(gV\Delta\rho)$ (where k_B is the Boltzmann constant, T is the temperature, g is the gravity acceleration, V is the particle volume, and $\Delta\rho$ is the specific mass contrast of the particle with the solvent), is of the order of 1 mm, like that of gibbsite disks. However, detailed modeling of this system is much more complicated than for gibbsite suspensions because the equation of state of charged nanosheets is much less understood than that of hard disks. A similar phase coexistence was also reported for

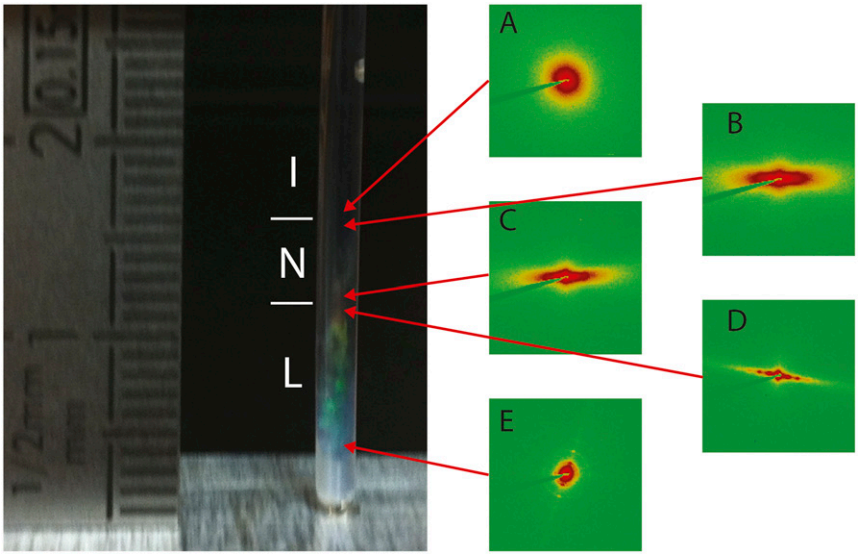

Fig. 4. A 2-mm-diameter X-ray capillary (size C, 0.49 wt %) was scanned from bottom to top, every 0.2 mm on the SWING SAXS beamline. Representative patterns are displayed: (*A*) isotropic phase just above the I–N interface, nematic phase (*B*) just below the I–N interface and (*C*) just above the N–L interface, (*D*) lamellar phase just below the N–L interface, and (*E*) in the middle of the lamellar phase region. (Note that in the photograph on the left, colored spots can be seen in the lamellar phase due to diffraction of visible light.)

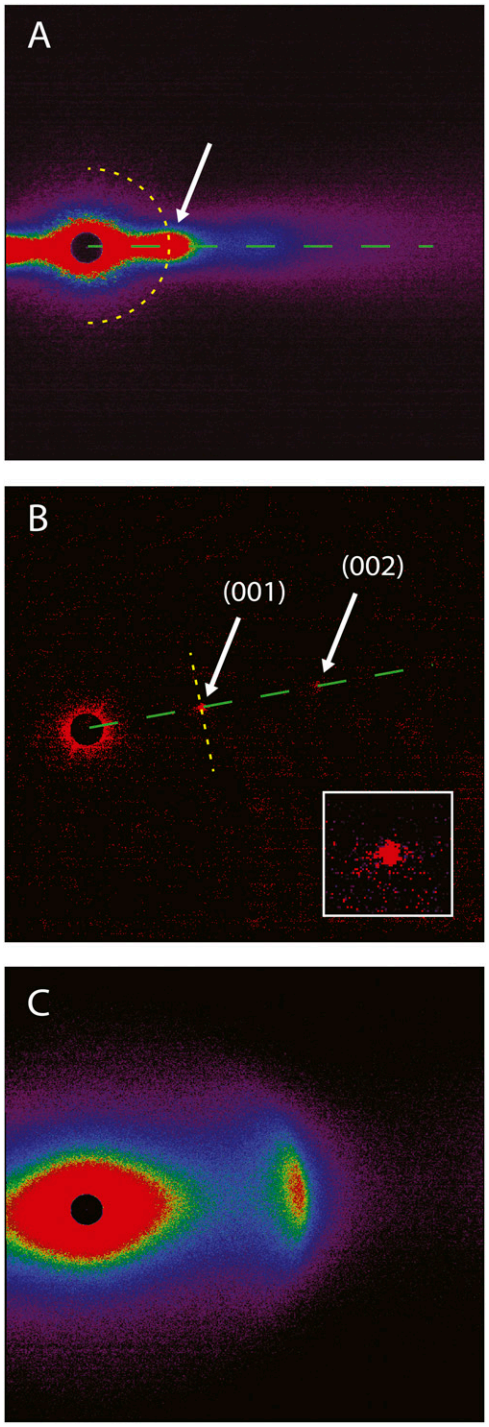

Fig. 5. High-resolution SAXS patterns recorded at the ID02 beamline of $H_3Sb_3P_2O_{14}$ nanosheet suspensions in the (*A*) nematic phase (size B, 0.18 wt %), (*B*) lamellar phase (size C, 0.24 wt %) [*Inset* is a magnified portion of the pattern showing the (001) reflection], and (*C*) nematic phase of a beidellite clay suspension (<D> = 280 nm, volume fraction $\phi = 0.8\%$). In *A* and *B*, the green dashed lines show the radial cuts through the patterns used to obtain the radial profiles of scattered intensity. In *A*, the yellow dotted half-circle shows the cut used to obtain the azimuthal profile and hence the nematic order parameter, and the yellow dotted line in *B* shows the cut used to obtain the transverse profile of the lamellar reflection.

suspensions of electrostatically stabilized goethite nanorods dispersed in water, and it was used to explore qualitatively a large part of the phase diagram in a single sample (26).

Description of Microscopic Textures. The coexistence of three different phases in the same sample was also observed in many flat capillary tubes by optical microscopy (Fig. 3*A*). For example, a sample of size C nanosheets, at 0.35 wt %, left undisturbed for several months in the field of gravity, displays three different liquid phases separated by sharp interfaces. The top phase is optically isotropic, whereas both the middle and bottom phases are birefringent and therefore liquid-crystalline. The middle phase is strongly homeotropically anchored on the glass surfaces so that it mostly looks dark in the polarizing microscope. Such homeotropic anchoring is expected for nematic suspensions of plate-like particles for entropic reasons (27). This alignment could easily be disturbed by applying a magnetic field of ∼800 mT delivered by small permanent magnets. After a minute, the texture became distorted, and the phase birefringence was revealed (*SI Appendix*, Fig. S3). After field removal, full homeotropic alignment of this mesophase was recovered after about an hour. In another sample that has weaker homeotropic anchoring, the middle phase shows a typical threaded texture (Fig. 3*B*), which strongly suggests that it is a nematic phase. This conclusion was indeed confirmed by SAXS experiments (see below). The nematic phase of $H_3Sb_3P_2O_{14}$ suspensions looks quite similar to that displayed by aqueous dispersions of $HSbP_2O_8$ (13), bentonite (28), beidellite, and nontronite natural clays (16). In contrast, the liquid-crystalline bottom phase did not show strong homeotropic anchoring and was not affected by the magnetic field, probably because it is more viscoelastic than the middle phase. Its optical texture (Fig. 3*C*) is also quite different because it is slightly reminiscent of the mosaic textures of ordered smectics (29). However, the texture is not typical enough to allow unambiguous identification of this mesophase, a task that requires X-ray scattering experiments.

Triphasic Capillary Tube Studied by SAXS. Representative SAXS patterns recorded while scanning a vertical capillary tube filled with a triphasic suspension of $H_3Sb_3P_2O_{14}$ are shown in Fig. 4. In the upper region, all patterns are typical of an isotropic phase, even just above the I/N interface (Fig. 4*A*). The next pattern in the series, just below this interface, is strongly anisotropic and presents broad peaks (d ∼ 230 nm); it is typical of an oriented nematic phase (Fig. 4*B*). Similar patterns were observed throughout the whole intermediate region till just above the bottom interface (Fig. 4*C*). Just below that interface and throughout the whole bottom region, very anisotropic patterns displaying sharp and intense diffraction peaks [with up to six equidistant (00l) orders] were recorded (Fig. 4 *D* and *E*). Such diffraction patterns strongly suggest the existence in this system of a lamellar phase, somewhat reminiscent of that of charged surfactant membranes diluted in pure water. The lamellar period decreases from 230 to 190 nm from top to bottom, due to the above-mentioned gravity-induced particle concentration gradient (*SI Appendix*, Fig. S2). In many scattering patterns, the X-ray reflections and diffuse peaks of both liquid-crystalline phases had maxima around the horizontal direction, which reveals some alignment of the nanosheets parallel to the capillary axis. This partial alignment may be due to flow during sample filling and/or slow nanosheet sedimentation under gravity.

High-Resolution SAXS. High-resolution SAXS experiments on selected samples allowed us to probe the large-scale structures of the different liquid-crystalline phases observed between crossed polarizers. Fig. 5*A* presents the X-ray scattering pattern of a well-aligned region of the middle phase. This pattern only shows broad scattering features arising from liquid-like positional correlations of the nanosheets. Because the pattern is also quite anisotropic, it is typical of a nematic phase, in agreement with the microscopic texture observations. A radial scan of the scattered intensity reveals two broad peaks whose scattering vector moduli are in a ratio of 1:2; they correspond to a period of

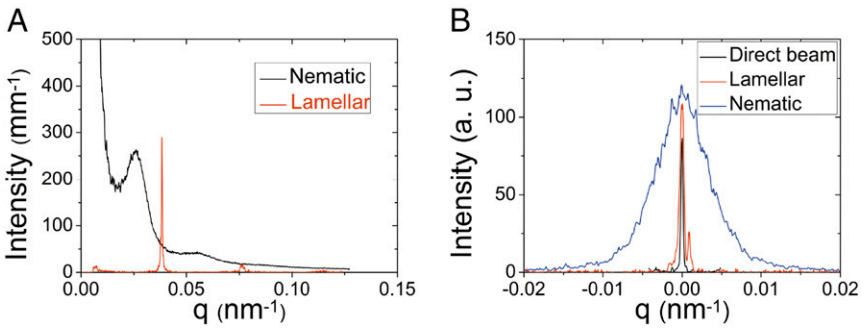

Fig. 6. (*A*) Radial profiles of scattered intensity drawn from the high-resolution SAXS patterns of the nematic and lamellar phases shown in Fig. 5. (The scattered intensity of the nematic phase has been divided by 2 for easier comparison.) (*B*) Transverse profiles drawn from the same scattering patterns. (The small peak at $q_{\perp} = 10^{-3}$ nm^{-1} in the scattering from the lamellar phase is due to another small domain in the beam.)

~240 nm (Fig. 6*A*). The broad peaks indicate a marked positional short-range order in the nematic phase which can then be regarded as a columnar nematic (Fig. 1*B*). The peak width in the perpendicular direction may be due to either the finite diameter of the nanoparticles or their orientational distribution, quantified by the nematic order parameter, S. Because the transverse width of the second-order broad peak is about twice that of the first, we conclude that the broadening of the peak is mostly due to the orientational distribution. Then, by neglecting in a first approximation the broadening due to the finite nanosheet diameter and by using classical methods, S can be estimated by fitting an azimuthal scan of the scattered intensity (*SI Appendix*, Fig. S4) going through the first scattering peak (30). The value obtained, $S = 0.93 \pm 0.05$, is very large but is not uncommon for colloidal nematic suspensions which usually show a strongly first-order I/N transition (3). This large value also suggests that the scattering essentially arises from a nematic single domain.

The high-resolution SAXS patterns of the other mesophase are completely different from those of the nematic phase. They usually show several very sharp dotted diffraction rings (*SI Appendix*, Fig. S5). Uniform rings were very rarely observed, whatever the sample treatment, so that good-quality, powder-like samples of the bottom phase could not be obtained. Nevertheless, by carefully scanning capillaries with the small X-ray beam, the scattering pattern of a single domain of this mesophase could be acquired for several samples (Fig. 5*B*). This pattern displays two very sharp diffraction spots that can be indexed as the (001) and (002) reflections from a one-dimensional ordered stack. A radial scan of the scattered intensity going through the (00l) reflections reveals sharp peaks whose width increases with l, as expected for a lamellar phase. The full-width at half-maximum (FWHM) of 5.3×10^{-4} nm^{-1} of the (001) peak in the radial direction is close to the experimental resolution (2.7×10^{-4} nm^{-1}) of the setup. A fit of the whole scattered intensity profile along the radial direction (*SI Appendix*, Fig. S6) was used to estimate the size of the lamellar domain along the director, $L_{//} \sim 25$ μm. The (001) lamellar reflection is thus quite different from the first broad scattering peak of the nematic phase which, with FWHM of 8.4×10^{-3} nm^{-1}, is ~16 times broader (Fig. 6).

Even though the radial profiles of scattered intensity in each phase differ so much, the distinction between the two types of organization depicted in Fig. 1 can only be made through the close inspection of the scattering profile of the reflections along the orthoradial direction. As mentioned above, for the nematic phase (Fig. 1*A*), this profile results from both the in-plane form factor of the nanosheets, leading to a widening of the reflection inversely proportional to the nanosheet diameter, and the orientational distribution, leading to the deformation of the reflection along a small circular arc. For the lamellar phase, neglecting the line broadening due to the Landau–Peierls instability of the lamellar phase (*SI Appendix*, Fig. S7) in a first approximation, the reflection width should be inversely proportional to the lamellar domain size, $L_{\perp}$, in the plane perpendicular to the director (Fig. 1*B*). In fact, the transverse scan of the scattered intensity going through the first reflection, shown in Fig. 5*B*, is barely wider than the experimental resolution function of the beamline (Fig. 6*B*). By simply applying Scherrer's formula (31), taking the experimental resolution into account, $L_{\perp}$ can be roughly estimated to ~20 μm. This size is much larger than the nanosheet diameter, $\langle D \rangle \sim 800$ nm for this sample, and leads to approximately $(20\ \mu m/800\ nm)^2 \sim 600$ nanosheets self-assembled to build up a smectic layer.

Because no other scattering feature could be detected, the nanosheets have no long-range positional correlations within the layers. This rules out the possibility of a smectic phase with solid-like layers (like smectic B, smectic E, smectic G, etc.) and allows us to identify the bottom phase as a usual lamellar phase of the same symmetry as the SmA of thermotropic liquid crystals and the L_{α} phase of surfactants.

For comparison, the SAXS pattern of a beidellite natural clay suspension, recorded in the same experimental conditions, is shown in Fig. 5*C*. This sample displays a clear nematic schlieren texture in polarized-light microscopy (16). Its SAXS pattern is indeed quite similar to that of the nematic phase of $H_3Sb_3P_2O_{14}$ suspensions (Fig. 5*A*), and it is completely different from that of the lamellar phase (Fig. 5*B*). Clay suspensions have not yet been reported to display any other mesophase than the nematic one because they undergo a sol/gel transition at concentrations only slightly larger than that of the isotropic/nematic transition, hence forbidding any higher order to take place at larger concentrations.

Detailed experimental studies of charged gibbsite, $Ni(OH)_2$, and layered double hydroxide nanoplates, of aspect ratio ~12–15, most often show that the nematic and columnar phases are more stable than the lamellar one (32–37). There is indeed only one report in literature of a lamellar phase in suspensions of gibbsite particles, but it is not based on the detailed analysis of the scattering from a single domain (38), and no lamellar/nematic phase coexistence was reported. However, the $H_3Sb_3P_2O_{14}$ nanosheet suspensions described here have much larger aspect ratios (>100) and therefore form liquid-crystalline phases at much smaller concentrations than these systems. Moreover, the electrostatic repulsions between nanodisks and nanosheets may strongly differ due to the higher anisotropy of the latter. There are also several reports of the existence of a lamellar phase in systems of nanosheets (14, 18, 39–42), but they all rely on the analysis of the scattering from unaligned (i.e., powder-like) samples. Indeed, none of these studies show the detailed analysis of the transverse profiles of the X-ray reflections from single domains of the lamellar phase, which is the most stringent criterion to tell the difference between a columnar nematic and a lamellar phase (Fig. 1). Moreover, $H_3Sb_3P_2O_{14}$ nanosheet suspensions are so far the only experimental system where both the columnar nematic and lamellar phases coexist in the same samples, which confirms that these phases have different structures. Nevertheless, the (isotropic–nematic–lamellar) phase sequence, upon increasing concentration, is quite robust in this system because it is observed for all four size fractions, A to D, of

$H_3Sb_3P_2O_{14}$ nanosheets. The phase transition concentrations decrease with increasing particle size (*SI Appendix, Text*), as already reported in previous studies (40).

Theoretical studies of colloidal suspensions of plate-like particles rarely predict the existence and stability of the lamellar phase with respect to the nematic and columnar ones (43, 44). For example, it was shown that disk polydispersity may enhance the stability of the lamellar phase. Moreover, there have only been a few theoretical studies of the phase diagram of electrically charged plate-like particles reported so far because the electrostatic interaction potential of two charged disks in suspension has only recently been calculated (45). Based on this potential, numerical simulations were made to draw rich phase diagrams that present the nematic and columnar phases, among others, but not the lamellar one (10, 46).

In this context, the observation of a lamellar phase in the suspensions of $H_3Sb_3P_2O_{14}$ nanosheets is somewhat surprising, and more theoretical work is needed to revise the phase diagrams of charged nanosheets. Other microscopic details could also play a role in the relative phase stabilities. For example, the chemical properties of atoms located at the nanoparticle rim are likely to differ from those of atoms on the particle faces, leading to differences in charge density that may affect the particle interactions, even at long range. Such particle heterogeneity that is reminiscent of patchy nanoparticles might affect the phase behavior of $H_3Sb_3P_2O_{14}$ suspensions (47, 48). Also, cation-mediated attractions between like-charged nanosheet rims might also take place. More experimental investigations are therefore needed to better characterize the surface properties at the particle rim and faces.

ACKNOWLEDGMENTS. We thank the following persons: (*i*) interns Nicolas Gauthier, Marine Le Meur, and Barbara Keller for assistance in synthesis and early characterizations; (*ii*) Dr. Laurent Michot and Dr. Erwan Paineau for providing us with the reference beidellite sample and Dr. Ivan Dozov and Dr. Johannes Theisen for help during the SAXS experiments; (*iii*) Dr. Javier Perez for assistance in using beamline SWING; and (*iv*) Dr. Theyencheri Narayanan and Dr. Sylvain Prevost for assistance in using beamline ID02. We acknowledge SOLEIL for provision of synchrotron radiation facilities (under the approved proposal 20141029) and European Synchrotron Radiation Facility (ESRF) for provision of synchrotron radiation facilities (under the approved proposal SC-4374). J.-C.P.G. and C.P. thank the Nanoscience program of the Commissariat à l'Énergie Atomique et aux Énergies Alternatives Nanoscience program for funding, as well as funding from the European Research Council (ERC) under the European Union's Seventh Framework Program (FP/2007-2013)/Grant Agreement 320915 "REE-CYCLE: Rare Earth Element Recycling with Low Harmful Emissions." J.-C.P.G. and P.D. thank the Agence Nationale de la Recherche for financial support, Grant ANR-17-CE04-0003.

1. De Gennes PG (1974) *The Physics of Liquid Crystals* (Clarendon Press, Oxford).
2. Frenkel D, Lekkerkerker HNW, Stroobants A (1988) Thermodynamic stability of a smectic phase in a system of hard-rods. *Nature* 332:822–823.
3. Vroege GJ, Lekkerkerker HNW (1992) Phase-transitions in lyotropic colloidal and polymer liquid-crystals. *Rep Prog Phys* 55:1241–1309.
4. Davidson P, Gabriel JC, Levelut AM, Batail P (1993) Nematic liquid-crystalline mineral polymers. *Adv Mater* 5:665–668.
5. Bolhuis P, Frenkel D (1997) Tracing the phase boundaries of hard spherocylinders. *J Chem Phys* 106:666–687.
6. Dogic Z, Fraden S (2006) Ordered phases of filamentous viruses. *Curr Opin Colloid Interface Sci* 11:47–55.
7. Nakata M, et al. (2007) End-to-end stacking and liquid crystal condensation of 6 to 20 base pair DNA duplexes. *Science* 318:1276–1279.
8. Grelet E (2014) Hard-rod behavior in dense mesophases of semiflexible and rigid charged viruses. *Phys Rev X* 4:021053.
9. Paineau E, et al. (2016) A liquid-crystalline hexagonal columnar phase in highly-dilute suspensions of imogolite nanotubes. *Nat Commun* 7:10271.
10. Jabbari-Farouji S, Weis JJ, Davidson P, Levitz P, Trizac E (2013) On phase behavior and dynamical signatures of charged colloidal platelets. *Sci Rep* 3:3559.
11. Morales-Anda L, Wensink HH, Galindo A, Gil-Villegas A (2012) Anomalous columnar order of charged colloidal platelets. *J Chem Phys* 136:034901.
12. Sasaki T, Watanabe M (1998) Osmotic swelling to exfoliation. Exceptionally high degrees of hydration of a layered titanate. *J Am Chem Soc* 120:4682–4689.
13. Gabriel JCP, et al. (2001) Swollen liquid-crystalline lamellar phase based on extended solid-like sheets. *Nature* 413:504–508.
14. Sun D, Sue HJ, Cheng Z, Martínez-Ratón Y, Velasco E (2009) Stable smectic phase in suspensions of polydisperse colloidal platelets with identical thickness. *Phys Rev E Stat Nonlin Soft Matter Phys* 80:041704.
15. Xu Z, Gao C (2011) Graphene chiral liquid crystals and macroscopic assembled fibres. *Nat Commun* 2:571.
16. Paineau E, et al. (2013) Liquid-crystalline properties of aqueous suspensions of natural clay nanosheets. *Liq Cryst Rev* 1:110–126.
17. Wang L, Sasaki T (2014) Titanium oxide nanosheets: Graphene analogues with versatile functionalities. *Chem Rev* 114:9455–9486.
18. Wong MH, et al. (2014) Solution processable iridescent self-assembled nanoplatelets with finely tunable interlayer distances using charge- and sterically stabilizing oligomeric polyoxyalkyleneamine surfactants. *Chem Mater* 26:1528–1537.
19. Li H, Wu J, Yin Z, Zhang H (2014) Preparation and applications of mechanically exfoliated single-layer and multilayer MoS_2 and WSe_2 nanosheets. *Acc Chem Res* 47:1067–1075.
20. Davidson P, Gabriel JCP (2005) Mineral liquid crystals. *Curr Opin Colloid Interface Sci* 9:377–383.
21. Griffith CS, Luca V, Cochrane J, Hanna JV (2008) Lanthanide/actinide ion-exchange and structural investigations of the layered phosphatoantimonic acid, $H_3Sb_3P_2O^{14}{\cdot}ZH_2O$. *Microporous Mesoporous Mater* 111:387–403.
22. Piffard Y, Lachgar A, Tournoux M (1985) Crystalline-structure of phosphoantimonate, $K_3Sb_3P_2O_{14}$. *J Solid State Chem* 58:253–256.
23. Van Vaerenbergh P, et al. (2016) An upgrade beamline for combined wide, small and ultra small-angle X-ray scattering at the ESRF. *Proceedings of the 12th International Conference on Synchrotron Radiation Instrumentation*, AIP Conference Proceedings, eds Shen Q, Nelson C (Am Inst Physics, Melville, NY), Vol 1741, p 030034.
24. Sano K, et al. (2016) Photonic water dynamically responsive to external stimuli. *Nat Commun* 7:12559.
25. van der Beek D, Schilling T, Lekkerkerker HNW (2004) Gravity-induced liquid crystal phase transitions of colloidal platelets. *J Chem Phys* 121:5423–5426.
26. Vroege GJ, Thies-Weesie DME, Petukhov AV, Lemaire BJ, Davidson P (2006) Smectic liquid-crystalline order in suspensions of highly polydisperse goethite nanorods. *Adv Mater* 18:2565–2568.
27. Reich H, Schmidt M (2007) Capillary nematization of hard colloidal platelets confined between two parallel hard walls. *J Phys Condens Matter* 19:326103.
28. Gabriel JCP, Sanchez C, Davidson P (1996) Observation of nematic liquid-crystal textures in aqueous gels of smectite clays. *J Phys Chem* 100:11139–11143.
29. Gray GW, Goodby JWG (1984) *Smectic Liquid Crystals: Textures and Structures* (L. Hill, London).
30. Paineau E, et al. (2012) In-situ SAXS study of aqueous clay suspensions submitted to alternating current electric fields. *J Phys Chem B* 116:13516–13524.
31. Guinier A (1994) *X-Ray Diffraction in Crystals, Imperfect Crystals, and Amorphous Bodies* (Dover Publications, New York).
32. Brown ABD, Ferrero C, Narayanan T, Rennie AR (1999) Phase separation and structure in a concentrated colloidal dispersion of uniform plates. *Eur Phys J B* 11:481–489.
33. Brown ABD, Clarke SM, Rennie AR (1998) Ordered phase of platelike particles in concentrated dispersions. *Langmuir* 14:3129–3132.
34. van der Beek D, Lekkerkerker HNW (2004) Liquid crystal phases of charged colloidal platelets. *Langmuir* 20:8582–8586.
35. Wijnhoven JE, Van't Zand DD, van der Beek D, Lekkerkerker HNW (2005) Sedimentation and phase transitions of colloidal gibbsite platelets. *Langmuir* 21:10422–10427.
36. Liu SY, et al. (2003) Liquid-crystalline phases of colloidal dispersions of layered double hydroxides. *Chem Mater* 15:3240–3241.
37. Mourad MCD, Devid EJ, van Schooneveld MM, Vonk C, Lekkerkerker HNW (2008) Formation of nematic liquid crystals of sterically stabilized layered double hydroxide platelets. *J Phys Chem B* 112:10142–10152.
38. Vis M, Wensink HH, Lekkerkerker HNW, Kleshchanok D (2015) Nematic and lamellar liquid-crystalline phases in suspensions of charged silica-coated gibbsite platelets. *Mol Phys* 113:1053–1060.
39. Yamaguchi D, et al. (2012) Aspect-ratio-dependent phase transitions and concentration fluctuations in aqueous colloidal dispersions of charged platelike particles. *Phys Rev E Stat Nonlin Soft Matter Phys* 85:011403.
40. Miyamoto N, Iijima H, Ohkubo H, Yamauchi Y (2010) Liquid crystal phases in the aqueous colloids of size-controlled fluorinated layered clay mineral nanosheets. *Chem Commun (Camb)* 46:4166–4168.
41. Geng F, et al. (2014) Gigantic swelling of inorganic layered materials: A bridge to molecularly thin two-dimensional nanosheets. *J Am Chem Soc* 136:5491–5500.
42. Geng F, et al. (2013) Unusually stable ~100-fold reversible and instantaneous swelling of inorganic layered materials. *Nat Commun* 4:1632.
43. Martínez-Ratón Y, Velasco E (2011) Effect of polydispersity and soft interactions on the nematic versus smectic phase stability in platelet suspensions. *J Chem Phys* 134:124904.
44. Tasios N, Dijkstra M (2017) A simulation study on the phase behavior of hard rhombic platelets. *J Chem Phys* 146:144901.
45. Agra R, Trizac E, Bocquet L (2004) The interplay between screening properties and colloid anisotropy: Towards a reliable pair potential for disc-like charged particles. *Eur Phys J E Soft Matter* 15:345–357.
46. Jabbari-Farouji S, Weis JJ, Davidson P, Levitz P, Trizac E (2014) Interplay of anisotropy in shape and interactions in charged platelet suspensions. *J Chem Phys* 141:224510.
47. Wensink HH, Trizac E (2014) Generalized Onsager theory for strongly anisometric patchy colloids. *J Chem Phys* 140:024901.
48. Petukhov AV, Tuinier R, Vroege GJ (2017) Entropic patchiness: Effects of colloid shape and depletion. *Curr Opin Colloid Interface Sci* 30:54–61.